Controlling carbon self-doping site of g-C$_3$N$_4$ for highly enhanced visible-light-driven hydrogen evolution

Yuanyong Huang, Di Li, Zhenyuan Fang, Ruijie Chen, Bifu Luo, Weidong Shi*

School of Chemistry and Chemical Engineering, Jiangsu University, Zhenjiang 212013, PR China

ABSTRACT

Nowadays, the C-substitution for N in g-C$_3$N$_4$ can promote π-electron availability and thus considerably increase its photocatalytic properties. However, the replacement of N in triazine ring of g-C$_3$N$_4$ by carbon atom represents a huge challenge on account of the higher electronegativity of N over C. Herein, we firstly report a simple and effective strategy for skillfully replacing one nitrogen with carbon atom by copolymerizing π-electrons-rich uracil with dicyandiamide via a facile Schiff-base reaction. The results show that direct incorporation C$_4$N$_2$ ring into the framework not only maintains the structural features of g-C$_3$N$_4$ and narrows its bandgap from 2.75 to 2.58 eV, but also effectively boosts the dissociation of photogenerated excitons. Consequently, C-incorporated g-C$_3$N$_4$ could harvest more solar light (λ = 750 nm). As expected, the photocatalytic hydrogen evolution rate of the optimal C self-doped g-C$_3$N$_4$ is almost as high as 13 and 20 times that of bare g-C$_3$N$_4$ under the visible-light exposure and the blue light illumination, respectively. Most importantly, the optimal sample also shows excellent performance under the green (λ = 500 nm) and yellow (λ = 550 nm) light illumination (94.07 and 28.47 μmol g^{-1} h^{-1}, respectively). This work sheds light on a subtle molecular-tailored protocol for controlling carbon self-doping site of the g-C$_3$N$_4$ to optimize the intrinsic electronic properties and photoactivity.

1. Introduction

Solar driven water-splitting, as a type of "green" technology, has been widely identified as a promising avenue to address energy and environmental crisis [1–4]. Since the discovery of photolysis of water into H$_2$ in 1972 by Honda and Fujishima [5], persistent efforts have been devoted to hunt for more efficient and environmentally sustainable photocatalysts. Recently, graphitic carbon nitride (g-C$_3$N$_4$) has sparked immense interest by virtue of the proper band position, photochemical durability and natural abundance [6–8]. Nevertheless, the photocatalytic activity of bulk g-C$_3$N$_4$ (BCN) is restricted by its limited surface area, fast recombination of photoinduced charge carriers and marginal visible-light absorption (λ < 470 nm) [9–12]. Therefore, various of approaches have been developed to boost the photocatalytic performance such as copolymerization [13], coupling with other semiconductors [14], element doping [15], engineering nanoarchitectures [16].

Presently, element doping is reckoned as an effective strategy to regulate the band structure and extend optical absorption range [17]. The doping of g-C$_3$N$_4$ with nonmetallic element (B, P, S, I) [18–21] and metallic element (K, Fe, Cu, W) [22–24] can effectively tune optical/electronic properties, yet also brings about external energy loss due to

forming new recombination centers of photogenerated carriers [25]. Fortunately, self-doped g-C$_3$N$_4$ not only can adjust intrinsic optical/electronic aspects, but also avoid to introduce exotic impurity and defects [26]. Typically, self-doped g-C$_3$N$_4$ can be compartmentalized into two types: C-rich and N-rich, which shows different optoelectronic properties and photocatalytic abilities [15]. In contrast to N self-doped g-C$_3$N$_4$, C-incorporated g-C$_3$N$_4$ holds great promise for ameliorating photoactivity, which the introduction of low electronegativity C not only can facilitate electronic conductivity, but also play the role of donor or acceptor to enhance photogenerated carrier dissociation. Depending on the synthetic methods, the sites and patterns of C self-doping among the network of g-C$_3$N$_4$ are different and thereby render its physicochemical properties distinctive. For instance, Che et al. manifested that carbon ring (Cring) was seamlessly stitched into the network of g-C$_3$N$_4$ by copolymerization of melamine and glucose to induce a strong in-building electric field for accelerating the photocarriers transfer kinetics [25]. In addition, Dong et al. demonstrated that the substitution of bridging N in triazine ring with C atoms could form delocalized big π-bonds through the calcination of melamine pretreated with absolute ethanol, which enhances electronic conductivity and photocatalytic performance [27]. Thus, it is highly efficient to incorporate C among the framework of g-C$_3$N$_4$ for tailoring its

---

electronic structure and photocatalytic activity. However, to the best of our knowledge, the control of C self-doping site in the matrix of g-C_3N_4 for enhancing visible-light photocatalytic H_2 production has not yet been reported.

Inspired by the Schiff-base chemistry, herein, we report a simple and effective strategy for skillfully replacing one nitrogen with carbon atom by copolymerizing π-electrons-rich uracil with dicyandiamide for the first time. The introduction of C_4N_2 ring into the g-C_3N_4 structure not only can improve the π-electron availability and shrink the bandgap, but also remarkably hamper the recombination of photo-induced carriers. As a result, such C-incorporated g-C_3N_4 shows superior optical adsorption up to 750 nm. In addition, the high up-shift of conduction band results in a robust thermodynamic driving force for the photocatalytic proton reduction. As expected, the photocatalytic hydrogen evolution rate of the optimal C self-doped g-C_3N_4 are almost as high as 13 and 20 times that of pristine g-C_3N_4 under the visible-light exposure and the blue light illumination, respectively. Besides, the $CNU_{0.075}$ exhibits an excellent photocatalytic performance under the green (λ = 500 nm) and yellow (λ = 550 nm) light illumination (94.07 and 28.47 $\mu mol\ g^{-1}\ h^{-1}$, respectively). This work provides a flexible method to skillfully control C self-doping site of g-C_3N_4 for ameliorating optical/electronic properties and photoactivity.

2. Experimental sections

2.1. Preparation of sample

The C-incorporated g-C_3N_4 samples were fabricated via mixing dicyandiamide (3.0 g) into different amounts of uracil (0.05 g, 0.075 g, 0.10 g) in 15 mL water under ultrasonic bath for 5 min, and then obtained white viscous suspensions were heated at 100 °C for 24 h in the Teflon-lined autoclave. Subsequently, the obtained precursors were dried at 60 °C for overnight to completely remove water. Afterwards, the final products were then obtained by calcination of mixed resultants at 550 °C for 4 h using a 50 mL alumina crucible with a cover. For simplicity, the as-prepared samples are labeled as CNU_x, where *x* stands for the initial mass of uracil added. To compare structural difference of the traditional carbon nitride and C-self doped g-C_3N_4, the BCN was also prepared via direct calcination method. Specifically, 3 g of melamine was calcined at 550 °C for 4 h in a muffle furnace under the same condition. After naturally cooling to ambient temperature, the resultant solids were thoroughly grinded into powder and collected for further exploration and characterization.

2.2. Physicochemical characterization

X-ray diffraction (XRD) was carried out the D/MAX-2500 diffractometer (Rigaku, Japan). Fourier transform infrared (FT-IR) was performed on the Nexus 470 (Thermo Electron Corporation). The transmission electron microscopy (TEM) was recorded on the Tecnai G2 F30 S-TWIN. The surface areas were measured by N_2 adsorption-desorption at 77 K (Micromeritics TriStar II 3020 analyzer). X-ray photoelectron spectroscopy (XPS) data were collected by the Thermo ESCALAB 250X (American). The solid-state ^{13}C nuclear magnetic resonance (NMR) information was obtained on a Switzerland Bruker model 600 M spectrometer. Elemental Analyzer was conducted on the FLASH1112A (America). The ultraviolet-visible diff ;use reflectance spectra (UV–vis DRS) were acquired by the Shimadzu UV-2450 spectrophotometer. The photoluminescene (PL) were implemented by the QuantaMaster™ 40 spectrometer. Electron paramagnetic resonance (EPR) was executed at a Bruker model A300 spectrometer at room temperature. The time-resolved PL spectra were tested to analyse the lifetime of charge carriers by the Edinburgh fls1000.

2.3. Photoelectrochemical measurements

The photoelectrochemical analysis was operated by the CHI -852C (Chenhua, China) electrochemical workstation with a conventional three-electrode setup and employed to measure transient photocurrent behavior of the photocatalysts, where the prepared electrodes were immersed in a sodium sulfate electrolyte solution (0.5 M), Pt wire and Ag/AgCl electrode (saturated KCl) acting as the working, counter and reference electrode, respectively. In a typical process, 100 mg of as-obtained catalysts were dispersed in a 3 mL ethanol solution adding into the 0.01 g of PVP (K30, M_w = 40,000) and 0.03 mL of oleic acid. Afterwards, the as-prepared solution was stirred continuously 1 h. Then, the slurry was gradually coated onto a clean 1 cm × 2 cm fluorine-doped tin oxide (FTO) glass electrode using a spin coater (MODEL KW-4A, Shanghai, China). Photocurrent measurements were recorded by a 300 W Xenon lamp (the light intensity is 47 mW/cm²). The electric capacity was tested to acquire Mott-Schottky plots for working electrodes at potential window ranged from −1.0 to 1.0 V, and the perturbation signal was an AC voltage magnitude of 50 mV with the frequency at 1, 2, 3 kHz, respectively. Electrochemical impedance spectra (EIS) was operated at an electrode potential of 0.3 V with a scan rate 25 mV s^{-1}. All measurements were performed at the room temperature.

2.4. Photocatalytic measurements

The photocatalytic reactions were carried out by a 200 mL Pyrex top-irradiation reactor and sealed with a rubber septum. The system was evacuated by N_2 bubbling into the dispersion for 30 min to remove air thoroughly and the temperature was carefully maintained below 5 °C under the experiment. Typically, 0.05 g catalyst was dispersed in 100 mL of an aqueous triethanolamine (TEOA) solution (10 vol%) as a sacrificial electron donor and the photodeposition of ∼3 wt% Pt cocatalyst was executed by directly adding trace $H_2PtCl_6 \cdot 6H_2O$ into the above 100 mL reaction solution using a 1 mL pipette. Before the reactions, the solution needs to be sonicated for 5 min. Next, the system was stirred continuously and illuminated by using a 300 W Xenon arc lamp coupled with band pass filters (λ = 420, 475, 500, 550 nm). Afterwards, the generated H_2 data were collected by the Shimadzu GC-14C gas chromatograph. Moreover, the injection port, column, and detector temperatures are 120, 80, and 180 °C, respectively. Besides, the recycle test was operated by using a gas closed circulation system and a 300 W xenon lamp equipped with band pass filters (λ = 475 nm and λ > 420 nm) under the same condition. Specifically, the reaction system was vacuumed every four hours and the generated H_2 data was recorded at intervals of 1 h by totally cycling test for 16 h.

3. Results and discussion

3.1. Chemical structure, crystal phase and microstructure

The incorporation of C=C building blocks from uracil aromatic monomer into the g-C_3N_4 structure was fabricated (Fig. 1a and Fig. S1). The possible polymerization process to generate g-C_3N_4 was proposed in the Fig. S2. The XRD and FT-IR were conducted to collect information about the chemical structures of as-prepared samples. All of the samples exhibit two distinct characteristic peaks at around 13.0° and 27.0° (Fig. 1b), which can be respectively assigned to the in-plane repeated units (100) and interlayer stacking of conjugated aromatic system (002) [9,28]. Besides, as shown in Fig. S3, the (002) peaks of the as-obtained CNU samples are slightly blue-shifted to 27.06° than the BCN (27.47°), revealing the increasing of adjacent-layer gap from d = 3.24 Å for BCN to d = 3.29 Å for $CNU_{0.10}$. In addition, the (002) peaks of as-synthesized products become broaden and weaker with increasing the amount of uracil, which demonstrates the disturbance of graphitic structure through partial substitution of N by C in the matrix
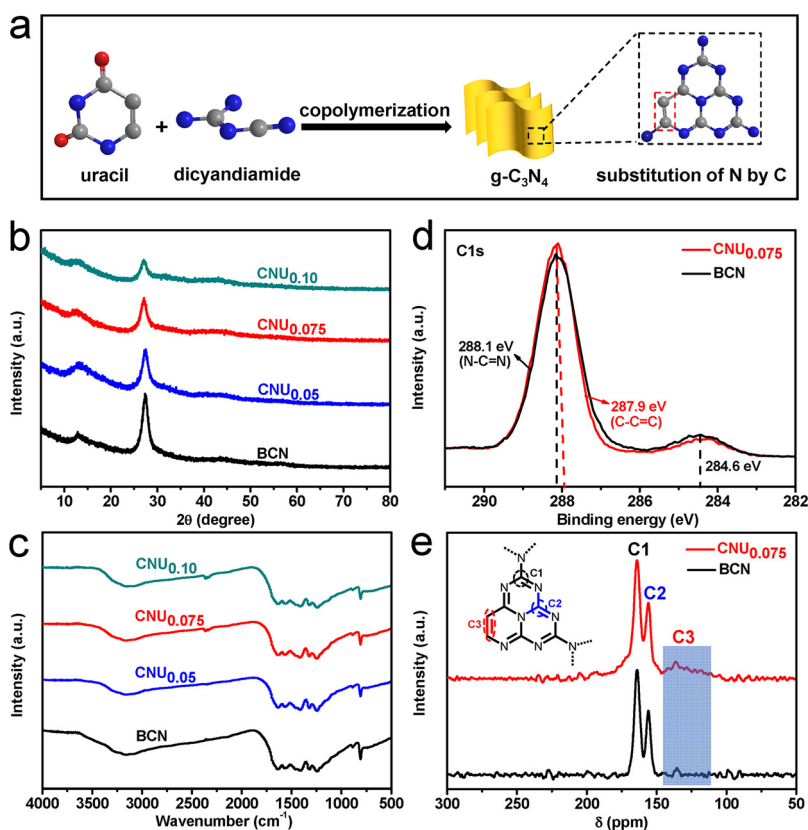
Fig. 1. (a) The substitution of bridging N in triazine ring of g-C_3N_4 with carbon atom (C, N and O atoms are denoted by gray, blue and red balls, respectively); (b) XRD patterns; (c) FT-IR spectra; (d) the C1s XPS analysis; (e) the solid-state ^{13}C NMR spectrum (For interpretation of the references to colour in this figure legend, the reader is referred to the web version of this article).

[29]. The FT-IR characteristic peaks for the uracil-treated samples are similar to the BCN, implying the basic chemical frameworks of CNU are retained (Fig. 1c). The typical peaks around 810, 1200–1650, 3000–3600 cm^{-1} are respectively ascribed to out-of-plane bending vibration characteristic of triazine rings, stretching modes of aromatic CN heterocycles and vibrating modes of −OH or −NH$_2$ [6,30].

To get clear proofs of the difference in chemical structure of the CNU$_{0.075}$ and BCN, XPS analysis and the solid-state ^{13}C NMR spectra were carried out. As exhibited in Fig. S4a and EDX elementary mapping (Fig. S6h, i, j), three elements (C, N and O) were detected in CNU$_{0.075}$, similar to BCN. The O1s peaks in CNU$_{0.075}$ and BCN are attributed to surface-absorbed CO$_2$ or H$_2$O [31]. In addition, as shown in Fig. 1d, it is found that one carbon species of CNU$_{0.075}$ with the binding energy at 287.9 eV is ascribed to the sp^2-bound carbon (C−C=C), while BCN at 288.1 eV is assigned to N−C=N [32,33]. The both of CNU$_{0.075}$ and BCN with binding energy at 284.6 eV are attributed to carbon impurities. Meanwhile, four distinctive peaks of BCN and CNU$_{0.075}$ sample can be observed in the deconvoluted N1s feature peak (Fig. S4c and S4d). The peaks at 398.4, 399.6, 400.8 and 404.2 eV can be ascribed to sp^2 hybridized nitrogen, tertiary N groups (N–(C)$_3$), −NH groups and charging effects, respectively [34,35]. These results suggest that the chemical framework of CNU$_{0.075}$ is basically maintained. Then, the chemical skeletons and element composition of CNU$_{0.075}$ were further investigated via the solid-state ^{13}C NMR spectra. As exhibited in Fig. 1e and Fig. S5, in contrast to the BCN, CNU$_{0.075}$ shows three distinct peaks. The two strong peaks at 164.098 ppm and 155.919 ppm are relating to the chemical shifts of C1 atom [CN$_2$−(NH$_x$)] and C2 atom (CN$_3$), respectively [29,33]. And the weak peak locating at $\delta \approx 136.368$ ppm is attributed to C3 atoms of the sp^2 C=C electron-withdrawing group. Besides, elemental analysis shows the C/N molar ratio of 0.745 for CNU$_{0.075}$, which is higher than that of BCN (0.667) (Table S2). The higher C content in CNU$_{0.075}$ is direct evidence for introducing C into the framework of g-C_3N_4. The C/N molar ratio is 0.667 for pristine BCN and gradually increases to 0.753 for CNU$_{0.10}$. Clearly, the elemental

analysis validates the effective incorporation C into the network of g-C_3N_4.

The surface morphology and texture of the BCN and CNU$_{0.075}$ were detected by the transmission electron microscope. As shown in Fig. S6, according to the TEM images, the as-prepared CNU$_{0.075}$ displays platelet-like structure, which is parallel to the BCN (Fig. S6a), indicating that the modification by copolymerization with uracil does not apparently change the morphology of BCN. From the HRTEM and selected area electron diffraction (SAED), CNU$_{0.075}$ presents an ideal Moiré pattern, revealing its amorphous structure with short-range atomic order, which is similar to BCN. In addition, the BET was employed to investigate surface area of the samples. As shown in Fig. S8a and S8b, the N$_2$ adsorption–desorption isotherms for the BCN and CNU$_{0.075}$ show classical type IV characteristics (H1-type hysteresis loop) [36]. The specific surface area and pore volume of CNU$_{0.075}$ were calculated to be 11.41 m^2/g and 0.052 cm^3/g, respectively, which were much closer to the BCN (10.52 m^2/g and 0.048 cm^3/g).

3.2. Optical absorption, bandgap and photocatalytic mechanism

The optical/electronic aspects could be evaluated via the UV–vis absorption spectra. As exhibited in the Fig. 2a, uracil-treated samples show a prominent redshift from 470 nm to the 750 nm in comparison with BCN, corresponding to the alteration of color from slightly yellow to light brown. The phenomenon could account for the incorporation of C=C chromophore in the g-C_3N_4 that evidently broadens the π-conjugated systems and thus narrows the semiconductor bandgap. The band gap energy of BCN, CNU$_{0.05}$, CNU$_{0.075}$, and CNU$_{0.10}$ are calculated through the Tauc method and evaluated to be 2.75, 2.69, 2.58, and 2.62 eV, respectively (the inset in Fig. 2a) [25,37]. Besides, the properties of BCN and CNU$_{0.075}$ such as the flat-band potential (E$_{FB}$), p/n conduction type and donor density were analysed by the Mott-Schottky (M–S) plot. Next, the E$_{FB}$ and charge density were calculated in the light of M–S formula [38]. The E$_{FB}$ of the semiconductor will be obtained
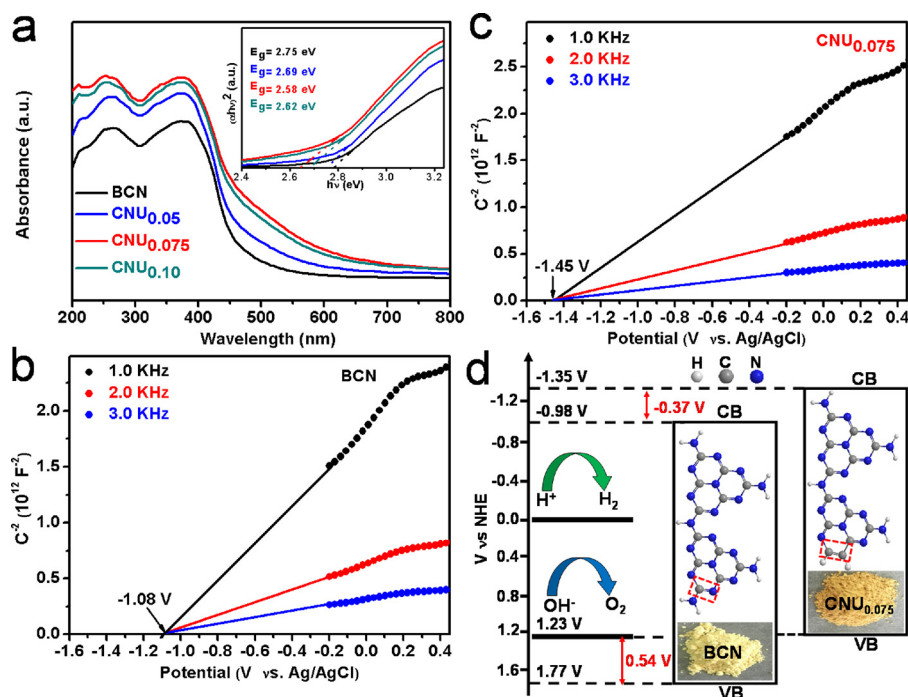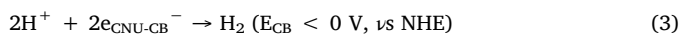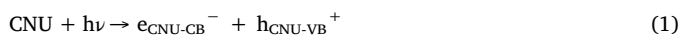
Fig. 2. (a) DRS. Inset: Tauc plots; (b) and (c) Mott-Schottky plots of BCN and $CNU_{0.075}$; (d) the schematic illustration of the energy band structure (BCN and $CNU_{0.075}$).

through the nodal increment of the fitting a regular line at $C^{-2} = 0$. As displayed in Fig. 2b and c, the E_{FB} are determined at -1.08 and -1.45 V for BCN and $CNU_{0.075}$ (vs. Ag/AgCl) by the M–S formula, which are converted into -0.88 and -1.25 V (vs. NHE), respectively. In addition, both $CNU_{0.075}$ and BCN show positive slops, indicating the n-type feature of semiconductor. For many n-type semiconductors, E_{FB} is closely related to conduction band (CB) and deemed to be about 0.1 V below the CB [39,40]. So, the CB potentials of BCN and $CNU_{0.075}$ are evaluated to be -0.98 and -1.35 V. As illustrated in Fig. 2d, the CB position of as-obtained $CNU_{0.075}$ upshifts 0.37 V than the BCN sample, which holds an enhanced thermodynamic driving force for the photocatalytic proton reduction (seen also in Fig. S10) [30,41]. In addition, the valence band (VB) edges of BCN and $CNU_{0.075}$ could be estimated to be 1.77 and 1.23 V, respectively. Based on the above analyses, a possible mechanism for improved H_2 evolution activity was summarized [42,43]. Under the visible light, the possible reactions in photocatalytic process are proposed below:

$$CNU + h\nu \rightarrow e_{CNU\text{-}CB}^{-} + h_{CNU\text{-}VB}^{+} \qquad (1)$$

$$TEOA + h_{CNU\text{-}VB}^{+} \rightarrow TEOA^{+} \qquad (2)$$

$$2H^{+} + 2e_{CNU\text{-}CB}^{-} \rightarrow H_2 \ (E_{CB} < 0 \text{ V}, \nu s \text{ NHE}) \qquad (3)$$

As shown in Eqs. (1–3), the electron (e^{-}) and hole (h^{+}) play the essential roles in this photocatalytic hydrogen evolution process. The photo-excited electrons on the CB position will migrate to co-catalyst Pt owning to its electron-sink function [44] and then generate H_2, whereas the holes settling on the VB position will react with triethanolamine (TEOA) as a hole scavenger (Eq. (2)) [43].

3.3. Optical/electronic properties and charge separation

The separation and transport behaviors of charge carriers in photocatalysts were assessed by the PL emission spectroscopy. As exhibited in Fig. 3a, the main PL emission peaks of all samples approximately station at 465 nm. In comparison to the BCN, the PL peaks of the $CNU_{0.075}$ are obviously redshift, which is ascribed to the expansion of π-electron conjugated system by the incorporation of C=C organic

building blocks into the heptazine units [33]. This also confirmed the UV–vis DRS results. Moreover, it is believed that the lower PL intensity implies the effective separation of the excitons, causing higher photocatalytic H_2 production activity [45–47]. In addition, the EPR was further identified above results (Fig. 3b). Only one single Lorentzian line with a g value of 2.00397 for both BCN and $CNU_{0.075}$ samples was found, which can be assigned to the π-conjugated aromatic delocalization structure of BCN and $CNU_{0.075}$ [21,33]. As expected, the $CNU_{0.075}$ occupies an improved EPR signal in dark due to efficiently promoting the production of radical pairs [48]. To further understand the materials' photoinduced electron-hole pairs transfer ability, EIS and transient photocurrent test were further studied. As shown in Fig. 3c, the arc radius of $CNU_{0.075}$ in the EIS plot is much smaller than BCN, suggesting that the incorporating C=C building blocks in carbon nitride framework could highly enhance charge transport. Fig. 3d shows the photocurrent density-potential data of BCN and $CNU_{0.075}$ under the room temperature. The dark current densities in BCN and $CNU_{0.075}$ samples are both negligible. The $CNU_{0.075}$ possesses higher photocurrent density at around $1.6 \, \mu A \, cm^{-2}$, which is roughly at 4-fold that of BCN under the visible light illumination. The enhancement in the I_{ph} of $CNU_{0.075}$ over BCN indicates more forceful conductivity and charge density, leading to a higher photocatalytic performance [34,49]. The electrochemical testing results are consistent with the data of photocatalytic H_2 evolution rate, illustrating that the photo-irradiated excitons mobility of $CNU_{0.075}$ is promoted. To further understand the charge transfer process, the lifetimes of BCN and $CNU_{0.075}$ were carried out by time-resolved transient fluorescence decay spectroscopy, exhibiting an average lifetime of 7.01 ns and 6.38 ns, respectively (Fig. S11). The shorter lifetime in $CNU_{0.075}$ indicates a rapid transfer of photoinduced charge involved in the redox reaction in $CNU_{0.075}$, thereby dramatically boosting its photocatalytic H_2 evolution [50].

3.4. Photocatalytic activity and stability

The activity of various photocatalysts was evaluated by releasing H_2 reactions. As exhibited in Figs. S12a and S13, the photocatalytic hydrogen evolution rate of the $CNU_{0.075}$ is almost as high as 8.6 and 13
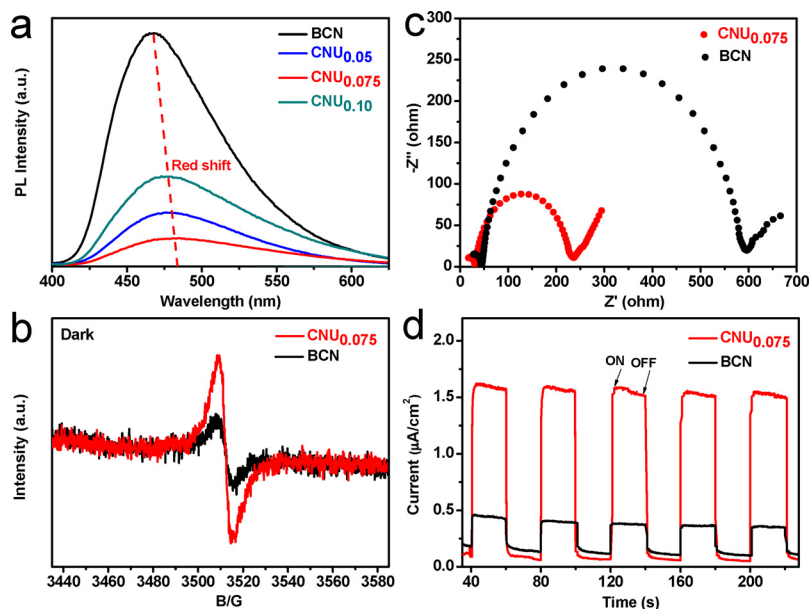
Fig. 3. (a) Room temperature (298 K) steady-state PL spectra; (b) EPR spectra of $CNU_{0.075}$ in the dark (BCN as a reference); (c) EIS Nyquist plots of BCN and $CNU_{0.075}$; (d) periodic on/off photocurrent response.
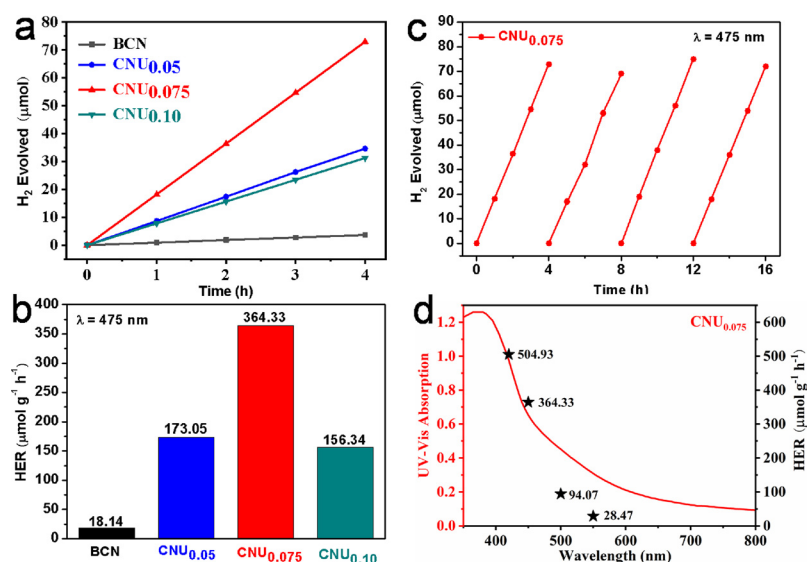

Fig. 4. (a) Photocatalytic H_2 release amount of the as-obtained samples ($\lambda = 475$ nm); (b) hydrogen evolution rate; (c) stability test of the $CNU_{0.075}$; (d) UV/Vis light absorption spectra of $CNU_{0.075}$ (left axis), and wavelength dependence of H_2 evolution rate with $CNU_{0.075}$ (right axis).

times that of bare g-C_3N_4 under the full arc (4243.62 µmol g^{-1} h^{-1}) and visible region (1003.94 µmol g^{-1} h^{-1}), respectively. Interestingly, as exhibited in Fig. 4a and b, under the blue light ($\lambda = 475$ nm), the $CNU_{0.075}$ shows an enhanced photocatalytic hydrogen production activity of 364.33 µmol g^{-1} h^{-1}, which is nearly 20 times higher than the pristine BCN (18.14 µmol g^{-1} h^{-1}). Moreover, through the consecutive four cycles of photocatalytic reaction, the $CNU_{0.075}$ is no obvious deactivation under the continuous blue light irradiation and visible-light illumination, which is due to the outstanding structure stability (Fig. 4c and Fig. S12b). In addition, Fig. S14 presents the XRD patterns of the $CNU_{0.075}$ sample before and after the photocatalytic reaction. It can be seen that the phase structure of the photocatalyst has no evident alteration after cycling test, further suggesting its superior stability. After 16 h operations, 291.46 µmol H_2 was obtained by the $CNU_{0.075}$ under the blue light ($\lambda = 475$ nm) and the turnover number (TON) concerning the Pt co-catalyst was calculated at 37.90 [48]. As reflected in Fig. 4d, the $CNU_{0.075}$ also exhibits good photoactivity with green

($\lambda = 500$ nm) and yellow ($\lambda = 550$ nm) light (94.07 and 28.47 µmol g^{-1} h^{-1}, respectively), further elucidating that $CNU_{0.075}$ could captured more photons in the photocatalytic process. The physicochemical properties and photocatalytic activity of some reported C-incorporated g-C_3N_4 in recent years were listed in Table 1. Indeed, the incorporation of low electronegativity of C-atom could effectively enhance the optical/electronic properties and photoactivity. However, it still remains a challenge to control carbon self-doping in the specific site of the network of g-C_3N_4.

Based on the above analysis, we assume that the following factors are responsible for the much greater photocatalytic performance of $CNU_{0.075}$ than BCN (see the Table S2). First, the effective introduction of C=C skeleton into framework of g-C_3N_4 ($CNU_{0.075}$) shows lower PL intensity, improved EPR signal in dark, higher photocurrent density, smaller impedance and shorter PL lifetime in comparison with BCN, which indicates that significantly enhances dissociation efficiency of photogenerated excitons and electron delocalization. Second, $CNU_{0.075}$

Table 1
Summary of the previously reported g-C_3N_4 concerning about C-incorporated sites and their activity increased factors/bulk g-C_3N_4 (N/A: no applicable).

Precursors	E_g (eV)	Application	Enhanced factors/pristine	C-incorporated sites	Ref.
melamine + ethanol	2.65	H_2 evolution	1.42 (λ > 420 nm)	substitution of bridging N with C atom (uncontrollable)	[27]
melamine + glucose	2.78	H_2 evolution	10 (λ > 420 nm)	incorporation of C-ring into the g-C_3N_4 (uncontrollable)	[25]
melamine + TAP	2.59	NO removal	1.48 (λ > 420 nm)	C-self doped in the specific site of g-C_3N_4 (controllable)	[10]
urea + C dots	2.60	H_2 evolution	2.4 (λ > 420 nm)	carbon quantum dot implanted g-C_3N_4 (uncontrollable)	[38]
graphene + dicyandiamide	N/A	optoelectronic application	300% (anodic photocurrent)	non-covalent doping of g-C_3N_4 with graphene (uncontrollable)	[11]
Urea + 1,3,5-cyclohexanetriol	2.56	H_2 evolution	21 (λ > 420 nm)	gradual doping graphited C ring within g-C_3N_4 (uncontrollable)	[15]
bulk g-C_3N_4 + glucose	2.18	H_2 evolution	3 (λ > 420 nm)	substitution of -NH among the triazine by C (uncontrollable)	[17]
C dots + urea	2.77	MO degradation	N/A	C quantum dots incorporated g-C_3N_4 (uncontrollable)	[37]
dicyandiamide + 2,6-diaminopyridine	2.26	H_2 evolution	2.16 (λ > 420 nm)	incorporation of pyridine ring into the g-C_3N_4 (controllable)	[28]
dicyandiamide + uracil	2.58	H_2 evolution	13 (λ > 420 nm) 20 (λ = 475 nm)	substitution of bridging N with C atom (controllable)	This work

can effectively absorb more extensive solar spectrum up to 750 nm (Fig. 2a) and thus shows excellent performance under the blue, green and yellow light (Fig. 4d). Finally, the conduction band of $CNU_{0.075}$ shifts up 0.37 V, which is thermodynamically more conducive to proton reduction to evolve H_2.

4. Conclusions

Inspired the Schiff-base chemistry, the substitution of N by C among the triazine was successfully constructed via the copolymerization of dicyandiamide and uracil. Such C-incorporation not only improves the π-electron availability and shrinks the bandgap of g-C_3N_4, but also effectively impedes the recombination of photogenerated carriers. Consequently, C-incorporated g-C_3N_4 shows superior optical adsorption up to 750 nm. The photocatalytic hydrogen evolution rate of $CNU_{0.075}$ is almost as high as 13 and 20 times that of bare g-C_3N_4 under the visible-light exposure and the blue light illumination, respectively. Besides, the $CNU_{0.075}$ also exhibits outstanding photoactivity under the green (λ = 500 nm) and yellow (λ = 550 nm) light illumination (94.07 and 28.47 μmol g^{-1} h^{-1}, respectively). In summary, this work offers an effective way for regulating C self-doped the site of g-C_3N_4 to optimize optical/electronic properties and photoactivity.

Acknowledgements

Appendix A. Supplementary data

Supplementary material related to this article can be found, in the online version, at doi:https://doi.org/10.1016/j.apcatb.2019.04.082.

References

[1] L.H. Lin, W. Ren, C. Wang, A.M. Asiri, J. Zhang, X.C. Wang, Appl. Catal. B: Environ. 231 (2018) 234–241.
[2] S.S. Yi, X.B. Zhang, B.R. Wulan, J.M. Yan, Q. Jiang, Energy Environ. Sci. 11 (2018) 3128–3156.
[3] Y.X. Fang, Y.T. Xu, X.C. Li, Y.W. Ma, X.C. Wang, Angew. Chem. Int. Ed. 57 (2018) 9749–9753.
[4] B.C. Qiu, M.Y. Xing, J.L. Zhang, Chem. Soc. Rev. 47 (2018) 2165–2216.
[5] A. Fujishima, K. Honda, Nature 238 (1972) 37–38.
[6] H. Wang, Y.R. Bian, J.T. Hu, L.M. Dai, Appl. Catal. B: Environ. 238 (2018) 592–598.
[7] Y.Z. Hong, E.L. Liu, J.Y. Shi, X. Lin, L.Z. Sheng, M. Zhang, L.Y. Wang, J.H. Chen, Int. J. Hydrogen Energy 44 (2019) 7194–7204.
[8] X.Q. Fan, L.X. Zhang, M. Wang, W.M. Huang, Y.J. Zhou, M.L. Li, R.L. Cheng, J.L. Shi, Appl. Catal. B: Environ. 182 (2016) 68–73.
[9] W. Iqbal, B.C. Qiu, Q.H. Zhu, M.Y. Xing, J.L. Zhang, Appl. Catal. B: Environ. 232 (2018) 306–313.
[10] W.K. Ho, Z.Z. Zhang, W. Lin, S.P. Huang, X.W. Zhang, X.X. Wang, Y. Huang, ACS Appl. Mater. Interfaces 7 (2015) 5497–5505.
[11] Y.J. Zhang, T. Mori, L. Niu, J.H. Ye, Energy Environ. Sci. 4 (2011) 4517–4521.
[12] S.S. Yi, J.M. Yan, B.R. Wulan, S.J. Li, K.H. Liu, Q. Jiang, Appl. Catal. B: Environ. 200 (2017) 477–483.
[13] J.S. Zhang, G.G. Zhang, X.F. Chen, S. Lin, L. Mohlmann, G. Dolega, G. Lipner, M. Antonietti, S. Blechert, X.C. Wang, Angew. Chem. Int. Ed. 51 (2012) 3183–3187.
[14] Z.P. Yan, Z.J. Sun, X. Liu, H.X. Jia, P.W. Du, Nanoscale 8 (2016) 4748–4756.
[15] Y. Yu, W. Yan, X.F. Wang, P. Li, W.Y. Gao, H.H. Zou, S.M. Wu, K.J. Ding, Adv. Mater. 30 (2018) 1705060.
[16] L.T. Ma, H.Q. Fan, J. Wang, Y.W. Zhao, H.L. Tian, G.Z. Dong, Appl. Catal. B: Environ. 190 (2016) 93–102.
[17] H.W. Wang, G.Q. Huang, Z.W. Chen, W.B. Li, Catalysts 8 (2018) 336.
[18] N. Sagara, S. Kamimura, T. Tsubota, T. Ohno, Appl. Catal. B: Environ. 192 (2016) 193–198.
[19] W. Chen, T. Liu, T. Huang, X. Liu, X. Yang, Nanoscale (2016) 3711–3719.
[20] C. Xu, Q. Han, Y. Zhao, L. Wang, Y. Li, L. Qu, J. Mater. Chem. A 3 (2015) 1841–1846.
[21] G.G. Zhang, M.W. Zhang, X.X. Ye, X.Q. Qiu, S. Lin, X.C. Wang, Adv. Mater. 26 (2014) 805–809.
[22] M. Zhang, X.J. Bai, D. Liu, J. Wang, Y.F. Zhu, Appl. Catal. B: Environ. 164 (2015) 77–81.
[23] Z. Li, C. Kong, G. Lu, J. Phys. Chem. C 120 (2016) 56–63.
[24] J. Ding, L. Wang, Q. Liu, Y. Chai, X. Liu, W.L. Dai, Appl. Catal. B: Environ. 176

(2015) 91–98.

[25] W. Che, W.R. Cheng, T. Yao, F.M. Tang, W. Liu, H. Su, Y.Y. Huang, Q.H. Liu, J.K. Liu, F.C. Hu, J. Am. Chem. Soc. 139 (2017) 3021–3026.

[26] J.W. Fang, H.Q. Fan, M.M. Li, C.B. Long, J. Mater. Chem. A 3 (2015) 13819–13826.

[27] G.H. Dong, K. Zhao, L.Z. Zhang, Chem. Commun. 48 (2012) 6178–6180.

[28] Z.H. Chen, P. Sun, B. Fan, Q. Liu, Z.G. Zhang, X.M. Fang, Appl. Catal. B: Environ. 170 (2015) 10–16.

[29] J.S. Zhang, X.F. Chen, K. Takanabe, K. Maeda, K. Domen, J.D. Epping, X.Z. Fu, M. Antonietti, X.C. Wang, Angew. Chem. Int. Ed. 49 (2010) 441–444.

[30] Z.Y. Fang, Y.Z. Hong, D. Li, B.F. Luo, B.D. Mao, W.D. Shi, ACS Appl. Mater. Interfaces 10 (2018) 20521–20529.

[31] G.G. Zhang, J.S. Zhang, M.W. Zhang, X.C. Wang, J. Mater. Chem. 22 (2012) 8083–8091.

[32] S.W. Cao, J.X. Low, J.G. Yu, M. Jaroniec, Adv. Mater. 27 (2015) 2150–2176.

[33] C. Yang, B. Wang, L.Z. Zhang, L. Yin, X.C. Wang, Angew. Chem. Int. Ed. 56 (2017) 6627–6631.

[34] J.W. Sun, J.S. Xu, A. Grafmueller, X. Huang, C. Liedel, G. Algara-Siller, M. Willinger, C. Yang, Y.S. Fu, X. Wang, Appl. Catal. B: Environ. 205 (2017) 1–10.

[35] Q. Han, B. Wang, Y. Zhao, C.G. Hu, L.T. Qu, Angew. Chem. Int. Ed. 54 (2015) 11433–11437.

[36] Z.K. Zhao, Y.T. Dai, J.H. Lin, G.R. Wang, Chem. Mater. 26 (2014) 3151–3161.

[37] J. Liu, Y. Liu, N.Y. Liu, Y.Z. Han, X. Zhang, H. Huang, Y. Lifshitz, S.T. Lee, J. Zhong, Z.H. Kang, Science 347 (2015) 970–974.

[38] Y. Wang, X.Q. Liu, J. Liu, B. Han, X.Q. Hu, F. Yang, Z.W. Xu, Y.C. Li, S.R. Jia, Z. Li,

[39] Angew. Chem. Int. Ed. 57 (2018) 5765–5771.

[39] S.M. Sun, W.Z. Wang, D.Z. Li, L. Zhang, D. Jiang, ACS Catal. 4 (2014) 3498–3503.

[40] Y.Z. Hong, C.S. Li, B.X. Yin, D. Li, Z.Y. Zhang, B.D. Mao, W.Q. Fan, W. Gu, W.D. Shi, Chem. Eng. J. 338 (2018) 137–146.

[41] Q. Han, F. Zhao, C.G. Hu, L.X. Lv, Z.P. Zhang, N. Chen, L.T. Qu, Nano Res. 8 (2015) 1718–1728.

[42] L.F. Cui, J.L. Song, A.F. McGuire, S.F. Kang, X.Y. Fang, J.J. Wang, C.C. Yin, X. Li, Y.G. Wang, B.X. Cui, ACS Nano 12 (2018) 5551–5558.

[43] A. Indra, P.W. Menezes, K. Kailasam, D. Hollmann, M. Schroder, A. Thomas, A. Bruckner, M. Driess, Chem. Commun. 52 (2016) 104–107.

[44] X.H. Zhang, T.Y. Peng, S.S. Song, J. Mater. Chem. A 4 (2016) 2365–2402.

[45] M.L. Li, L.X. Zhang, M.Y. Wu, Y.Y. Du, X.Q. Fan, M. Wang, L.L. Zhang, Q.L. Kong, J.L. Shi, Nano Energy 19 (2016) 145–155.

[46] L.X. Su, Q.Z. Huang, Q. Lou, Z.Y. Liu, J.L. Sun, Z.T. Zhang, S.R. Qin, X. Li, J.H. Zang, L. Dong, Carbon 139 (2018) 164–171.

[47] B.R. Wulan, S.S. Yi, S.J. Li, Y.X. Duan, J.M. Yan, Q. Jiang, Appl. Catal. B: Environ. 231 (2018) 43–50.

[48] Y.F. Li, R.X. Jin, Y. Xing, J.Q. Li, S.Y. Song, X.C. Liu, M. Li, R.C. Jin, Adv. Energy Mater. 6 (2016) 1601273.

[49] Z.W. Tong, D. Yang, Z. Li, Y.H. Nan, F. Ding, Y.C. Shen, Z.Y. Jiang, ACS Nano 11 (2017) 1103–1112.

[50] Y.F. Guo, J. Li, Y.P. Yuan, L. Li, M.Y. Zhang, C.Y. Zhou, Z.Q. Lin, Angew. Chem. Int. Ed. 55 (2016) 14693–14697.